IAC–24,C4,IP,20,x86908

Innovative Methodology for Evaluating Combustion Efficiency in Swirled Rocket Engines

Valerio Santolini[a*], **Christian Paravan**[b]

[a] *Space Propulsion Laboratory, Aerospace Science and Technology Department, Politecnico di Milano, Milan, 20156, Italy, valerio.santolini@polimi.it*
[b] *Space Propulsion Laboratory, Aerospace Science and Technology Department, Politecnico di Milano, Milan, 20156, Italy, christian.paravan@polimi.it*
[*] *Corresponding author*

Abstract

Swirl injection is a widely used strategy to improve performance in hybrid rocket engines. However, the gas flow can sometimes retain a tangential component when accelerating in the nozzle, leading to overestimated combustion efficiencies due to throat contraction. This work presents a new method capable of calculating corrected combustion efficiency for swirling flows, using pressure, mass flow rate, and thrust measurements. This method is applied to compute combustion efficiencies for multiple experimental tests, achieving a 100% convergence rate with results consistent with literature expectations.

Nomenclature

α	conical nozzle semi-angle	$^\circ$
Δm	fuel mass variation with the firing	kg
Δq	specific energy gas losses	J/kg
Δt	time window	s
ε	exit-on-throat area ratio	$-$
η_{c^*}	combustion efficiency	$-$
γ	specific heat ratio	$-$
λ	conical nozzle corrective factor	$-$
ρ	density	kg/m^3
Θ	temperature	K
$\zeta_{A_{th}}$	throat areas ratio	$-$
$\zeta_{\Theta_{fl}}$	flame temperatures ratio	$-$
A	area or surface	m^2
a	sonic speed	m/s
a_r	power law linear coefficient	$\frac{(m/s)}{(kg/m^2 s)^{n_r}}$
c^*	characteristic velocity	m/s
D	diameter	m
h	height	m
G	mass flux	$kg/m^2 s$
l	length	m
Ma	Mach number	$-$
Mm	molar mass	g/mol
$\dot{m}$	mass flow rate	kg/s
n_r	power law exponential coefficient	$-$
p	pressure	MPa
$\dot{Q}$	nozzle heat power losses	W
R	perfect gas constant	$J/kg\,K$
R^2	coefficient of determination	$-$
R_u	universal perfect gas constant	$J/mol\,K$
r	regression rate	mm/s
T	thrust	N
t	time	s
v	gas flow velocity	m/s
y	gas properties vector	
Z_{obj}	minimization function	$-$
z	nozzle axial coordinate	m or $-$

$_{amb}$	ambient (atmosphere-related)
$_b$	burning (firing)
$_{CEA}$	ideal
$_c$	chamber
$_{cl}$	measured at injection arm
$_e$	nozzle exit
$_f$	fuel-related
$_{lc}$	load cell
$_{new}$	new proposed method
$_{noz}$	nozzle-related
$_{old}$	old method
$_{ox}$	oxidizer
$_{real}$	experimental
$_{st}$	static (pre-firing)
$_{th}$	nozzle throat
$_{tot}$	total
$_v$	measured at vortex center

Acronyms/Abbreviations

ABS	Acrylonitrile-Butadiene-Styrene
CB	Carbon Powder
HRE	Hybrid Rocket Engine
NIST	National Institute of Standards and Technology
SPLab	Space Propulsion Laboratory
SEBS-MA	Styrene-Ethylene-Butylene-Styrene grafted with Maleic-Anhydride
SVFP	SPLab VFP
TOT	Thickness over Time
VFP	Vortex Flow Pancake

1. Introduction

Swirling injection is a widely implemented strategy to improve the performance of hybrid rocket engines (HRE) [1–3]. Traditional hybrid rockets suffer from slow solid-fuel regression rates, low volumetric loading, and relatively poor combustion efficiency. Swirl injection enhances performance by introducing a strong tangential velocity component to the oxidizer in the combustion chamber, resulting in increased regression rates and combustion efficiency [4–11]. The tangential velocity component tends to diminish as the flow moves toward the exit, as rocket nozzles are designed to accelerate gas in the axial direction. However, if the combustion chamber and post-chamber lengths are insufficient and the initial flow is highly swirled, the gas may retain its swirl as it expands through the nozzle [12–15]. Consequently, evaluating combustion chamber efficiency using traditional methods can lead to overestimation, with values potentially exceeding 100% [1, 16–18].

This work proposes a new approach for calculating combustion chamber efficiency in the presence of swirling flows. Typically, combustion chamber pressure, total mass flow rate, and throat area are used to compute the experimental characteristic velocity, c^*. In addition, the proposed method requires thrust measurement to apply the swirl correction. Thrust was chosen because it is a non-invasive and easily obtained measurement, compared to alternatives like combustion chamber temperature, which would provide more direct data but is challenging to measure due to the harsh environment. This method does not directly alter the calculation of combustion efficiency or characteristic velocity but applies a correction to the throat area, proportional to c^*.

The algorithm was tested using firing tests conducted at the Space Propulsion Laboratory (SPLab) of Politecnico di Milano with the Vortex Flow Pancake (VFP) engine. The VFP, characterized by strong tangential injection, produces a highly swirled flow, making it an ideal candidate to test the effectiveness of the developed method.

2. Experimental Setup

Multiple firing tests were conducted to evaluate the newly developed method using the VFP engine, selected for its ability to produce a highly swirled flow. The Space Propulsion Laboratory's VFP engine (SVFP) consists of two flat solid fuel disks encased in stainless steel rings. These disks are separated by a tangential injection device featuring four channels spaced evenly along the circumference, which are used initially for oxidizer injection and later for nitrogen purging. The space between the two fuel grains serves as the combustion chamber, whose height increases as the fuel regresses during combustion. The entire assembly is held together by top and bottom connection flanges, with O-ring gaskets at each junction, and is secured by four nuts and bolts. A convergent-divergent copper nozzle was employed, with an exit-to-throat area ratio of $\varepsilon = A_e/A_{th} = 2$. The nozzle is enclosed by a cooling chamber through which water flows during tests, using two pipes connected to the water supply system. This cooling process inevitably leads to some energy loss from the hot expanding gas mixture. However, this trade-off is considered worthwhile, as it significantly prolongs the nozzle's lifespan.

2.1 Materials and Fuels

The laboratory tests utilized various fuel compositions, categorized into two groups: acrylonitrile-butadiene-styrene (ABS) grains and paraffin-based grains. The paraffin-based category consists of paraffin mixed with varying percentages of thermoplastic materials. ABS grains were produced using 3D printing, while paraffin-based fuels were cast. The compositions tested are listed in Tab. 1.

ABS is a thermoplastic polymer selected for its favorable mechanical and thermal properties, as well as its ease of shaping via 3D printing [19–22]. Its enthalpy of formation is characterized in Ref. [22, 23], a key parameter for computing the characteristic velocity using the NASA-CEA code.

Paraffins are hydrocarbons with the general formula C_nH_{2n+2}. At room temperature, they can be either liquid, if $10 \leq n \leq 18$, or solid, if $18 \leq n \leq 55$ [24, 25]. Solid paraffins are further divided into macro-crystalline ($18 \leq n \leq 30$) and micro-crystalline waxes ($40 \leq n \leq 55$). Macro-crystalline waxes exhibit greater malleability and have melting points in the range of 313–333 K, whereas micro-crystalline waxes are more brittle, with melting points between 333–363 K [24, 25]. The

paraffin used in this study is SasolWax 0907, a commercial micro-crystalline wax produced by Sasol GmbH [26]. It is the primary component of the paraffin-based fuel formulations, and its brute chemical formula is $C_{50}H_{102}$. With a high melting temperature of 356–367 K and low melt layer viscosity, it is well-suited for hybrid rocket combustion due to its positive response to the entrainment effect [27]. By mixing paraffin with varying amounts of Styrene-Ethylene-Butylene-Styrene grafted with Maleic-Anhydride (SEBS-MA), a good balance is achieved between mechanical properties and ballistic performance. In this study, formulations with 5-10-20 % SEBS-MA by weight were tested.

SEBS-MA, a thermoplastic co-polymer commercially available from Sigma-Aldrich [28], serves as a reinforcing additive, improving the mechanical properties of the brittle paraffin matrix. Its compatibility with paraffin and its favorable mechanical and thermal properties make SEBS-MA an effective reinforcer. The melting temperature of SEBS-MA ranges from 455 to 460 K [28, 29]. SEBS-MA consists of styrene-ethylene-butylene-styrene blocks, grafted with 2 wt% maleic anhydride, linked to the butylene block. The central ethylene-butylene block imparts rubber-like flexibility, while the styrene blocks provide thermoplastic behavior. Adjusting the percentage of SEBS-MA in the mixture allows tuning of both mechanical properties and ballistic performance.

Carbon powder (CB), a micron-sized graphite powder supplied by Sigma-Aldrich [30], was added to all paraffin-based formulations at a concentration of 1 wt%. CB enhances radiant heat transfer between the flame and fuel surface, while also preventing excessive thermal wave penetration into the bulk fuel, which could degrade mechanical properties and cause grain sloughing [29]. The CB particles have a diameter of less than 20 μm and a density of 2100 kg/m^3 [30].

2.2 Test Stand

The experimental setup is equipped with several sensors and instruments to monitor key parameters during firing tests. A pressure sensor is mounted on one of the four injection arms to measure the pressure of the oxidizer, while a second pressure sensor is installed axially within the combustion chamber, opposite the nozzle, to capture chamber pressure. A load cell is positioned along the axis of thrust to measure the engine's thrust output, and an igniter is connected to one of the injection arms to initiate combustion. Additionally, a thermocouple is placed in the water duct that exits the nozzle to monitor the cooling water temperature. The feed system consists of two main channels: one for the oxidizer and the other for nitrogen purging. Both lines operate at a feeding pressure of 4 MPa. The oxygen flow rate is regulated by a mass flow meter, while several electrovalves ensure precise control of the lines, allowing for coordinated opening and closing immediately prior to combustion in the chamber.

3. Tests Data

During the tests, data on chamber pressure, oxygen mass flow rate, thrust, and temperature were collected and subsequently processed. The data was carefully filtered to retain meaningful small oscillations due to combustion instabilities while eliminating instrument noise for accuracy.

The burning window, Δt_b,is defined as the period starting when the pressure reaches 70% of its maximum value and ends at the oxygen shutdown. Fig. 1a displays an example of the filtered pressure trace, with p_{cl} representing the pressure at the injection arm and p_v the pressure at the bottom of the combustion chamber. The average pressure is computed over the burning window as:

$$\bar{p}_c = \frac{1}{\Delta t_b} \int_{\Delta t_b} p_c(t) dt \quad [1]$$

Similarly, the average oxidizer mass flow rate and average thrust are calculated as:

$$\dot{\bar{m}}_{ox} = \frac{1}{\Delta t_b} \int_{\Delta t_b} \dot{m}_{ox}(t) dt \quad [2]$$

$$\bar{T} = \frac{1}{\Delta t_b} \int_{\Delta t_b} T(t) dt \quad [3]$$

The net thrust, $T(t)$, is obtained by removing the static weight of the engine from the load cell measurement:

$$T(t) = T_{lc}(t) - \frac{1}{\Delta t_{st}} \int_{\Delta t_{st}} T_{lc}(t) dt \quad [4]$$

Here, Δt_{st} represents the time window for collecting static data, usually the first 9 seconds before oxygen flow begins. The temperature of the outflowing water from the nozzle's cooling chamber is monitored by a thermocouple. The temperature data, sampled at 1000 Hz, undergoes low-pass filtering with a cutoff frequency of 0.3 Hz to remove noise. Fig. 1b illustrates an example of a water temperature trace, showing raw data, a moving mean filter (using 101 points), and the final low-pass filtered signal.

The ballistic performance metrics obtained from the tests include the regression rate as a function of the total mass flux and the combustion efficiency, expressed in terms of the characteristic velocity. The regression rate is calculated using the thickness over time (TOT) method, which is based on the weight difference of the fuel grains before and after firing. Since the engine utilizes two fuel disks regressing simultaneously, the individual regression rates for both disks are computed and then averaged to ob-

Table 1. Tested formulations and theoretical maximum density.

ID	ABS	Sasol 0907	SEBS-MA	CB	ρ_f (kg/m^3)
ABS	100 wt.%	-	-	-	1050
W1	-	99 wt.%	-	1 wt.%	929
SEBS10	-	89 wt.%	10 wt.%	1 wt.%	928
SEBS20	-	79 wt.%	20 wt.%	1 wt.%	926

tain the final value. For a single disk *i*, the average regression rate is given by:

$$\bar{r}_{f_i} = \frac{\Delta m_i}{\rho_f A_{f_i} \Delta t_b} \quad [5]$$

where Δm_i is the mass difference for the grain, ρ_f is the fuel density and A_{f_i} is the burning surface area. The global average regression rate $\bar{r}_f$ is computed by averaging the individual values $\bar{r}_{f_i}$. The total mass flux through the combustion chamber is calculated using the fuel and oxidizer mass flow rates. The height of the combustion chamber changes as the fuel grains burn. This height can be approximated as a linear function of time:

$$h_c(t) = h_c(0) + 2\,\bar{r}_f \quad [6]$$

The average chamber height is taken as the mean of the initial ($t = 0$) and final ($t = \Delta t_b$) heights. The fuel and total mass flow rates are computed as

$$\dot{\bar{m}}_f = \Delta m / \Delta t_b \quad [7]$$

$$\dot{\bar{m}}_{tot} = \dot{\bar{m}}_f + \dot{\bar{m}}_{ox} \quad [8]$$

Thus, the mass flux is:

$$\bar{G}_{tot} = \frac{\dot{\bar{m}}_{tot}}{0.5\, D_f\, \bar{h}_c} \quad [9]$$

with D_f the fuel outside diameter.

The temperature trace recorded during the tests is used to calculate the average nozzle heat power losses $\dot{\bar{Q}}$, following the procedure described in Ref. [31]. The specific energy gas losses by passing through the nozzle are computed as:

$$\Delta q = \dot{\bar{Q}} / \dot{\bar{m}}_{tot} \quad [10]$$

This value is used to construct its antiderivative:

$$\Delta q = \int_0^{l_{noz}} \frac{\partial q(z)}{\partial z} dz \quad [11]$$

The combustion chamber efficiency is calculated based on the ratio of the characteristic velocity:

$$\eta_{c^*} = c^*_{real} / c^*_{CEA} \quad [12]$$

where velocity of reference, c^*_{CEA}, is the reference characteristic velocity obtained from NASA-CEA code, and c^*_{real} is derived from the experimental data:

$$c^*_{real} = \frac{\bar{p}_c\, A_{th}}{\dot{\bar{m}}_{tot}} \quad [13]$$

Here, A_{th} is the throat area of the nozzle, which plays a significant role in calculating the real characteristic velocity and, thus, the combustion efficiency. It will be discussed in the next section.

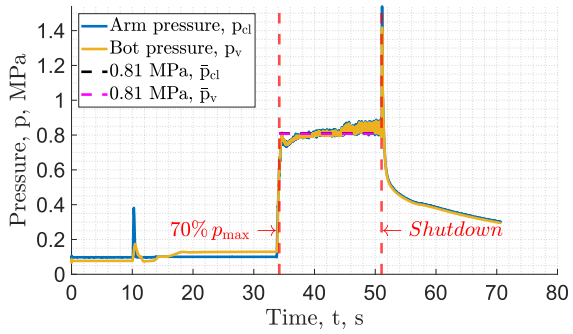

(a)

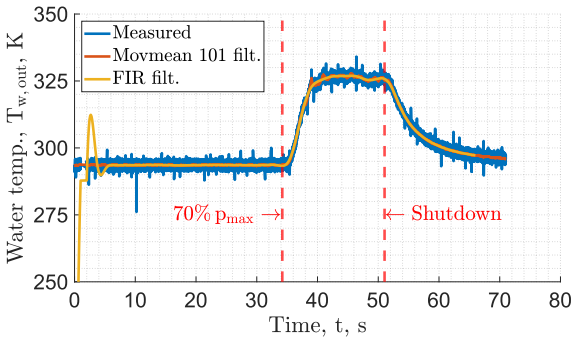

(b)

Fig. 1. Example of experimental data of (a) filtered pressure trace, with p_{cl} pressure at injection arm and p_v pressure at combustion chamber bottom and (b) temperature trace example: raw data, moving mean (movmean) filtering on 101 points, low-pass filtering.

4. Algorithm for Swirl Correction

This section presents the algorithm developed in this work. The objective of the algorithm is to use additional thrust data to estimate the effective throat area and, as a result, calculate an unbiased combustion efficiency. This work does not aim to solve the complex three-dimensional gas flow equations that describe the behavior of swirled flows through a nozzle, as these have been extensively studied in various works [12–15]. Instead, the proposed method simplifies the flow to a one-dimensional approximation, where the swirl effects are inferred from thrust measurements and reflected in the throat area. When calculating the characteristic velocity using Eq. [12], pressure and mass flow rate are directly measured (see Section 3), leaving the throat area as the only variable that may change. Goldman and Gany previously noted that "a reduction in the effective throat area of the nozzle" is a result of swirl effects [16]. The following sections offer a step-by-step explanation of the algorithm's structure. Also, the general workflow of the code is hereby presented in a logic similar to programming syntax, where indented lines represent the inner steps of the functions. This format is used throughout the subsequent subsections as well, to aid in understanding the algorithm more easily.

Syntax logic:

```
> setup input data
> characterize gas mixture:
    » run NASA-CEA to simulate combustion
    » rebuild CEA gas mixture using NIST data
    » return: gas mixture
> compute true throat area by minimizing objective errors:
    » find pressure and thrust error:
        » find computed pressure and thrust:
            » guess throat area and throat temperature
            » compute combustion chamber values (thus pressure):
                » integrate Shapiro's equations from throat to chamber
                return chamber values
            » compute exit values (thus thrust):
                » integrate Shapiro's equations from throat to exit
                return exit values
            return computed pressure and thrust
        return pressure and thrust error
    return throat area @ mimimum error
> collect and post-process output (thus new combustion efficiency)
```

4.1 Setup input data

Input data is categorized into two groups: mandatory and supplementary. Mandatory data is required for solving the equations and includes:

- Fuel and oxidizer properties: chemical composition, enthalpy of formation, and storage temperature.
- Oxidizer-to-fuel ratio.
- Measured chamber pressure.
- Measured thrust.
- Measured mass flow rate.
- Nozzle throat area.;
- Nozzle exit area (or exit-to-throat area ratio).

The fuel, oxidizer, and chamber pressure are essential for solving the combustion problem, while the pressure, thrust, and mass flow rate act as boundary conditions in solving the minimization equations. The throat and exit areas serve as geometrical constraints necessary for solving the nozzle problem.

Supplementary data, which enhances result accuracy, includes:

- Combustion chamber area.
- Heat losses.
- Nozzle 3D losses (e.g., conical divergent angle).

The combustion chamber area is an additional geometrical constraint, but can be replaced by the assumption of near-zero gas chamber velocity when solving the equations. Heat losses are useful in eliminating the assumption of an adiabatic nozzle, though assuming zero heat loss still allows the problem to be solved. Similarly, nozzle 3D losses refine the result but can also be assumed to be negligible, as with heat losses.

4.2 Gas mixture characterization

Using the reagent data, oxidizer-to-fuel ratio, and combustion chamber pressure, the NASA-CEA code can simulate the theoretical combustion outcome. This computation is necessary to obtain the theoretical characteristic velocity (c^*_{CEA}), as well as the composition of the combustion gases. Specifically, the mixture's specific heat ratio γ and molar mass Mm are required for subsequent calculations. While NASA-CEA provides the combustion gas species, the thermal properties of these species are sourced from the National Institute of Standards and Technology (NIST). A weighted average is then applied to calculate the mixture's γ and Mm values. This additional step allows for the mapping of thermal properties across a wide temperature range, enabling the use of a calorically imperfect gas model, $\gamma(\Theta)$, in the nozzle calculations. The specific heat ratio, tabulated from NIST data, is then approximated using a 7th-order polynomial. This polynomial approximation provides a functional representation of γ as a function of temperature, Θ. Additionally, the first-order derivative of

γ with respect to temperature, $\partial\gamma(\Theta)/\partial\Theta$, is expressed as a 6th-order polynomial.

Syntax logic:

> combustion = NASA_CEA(fuel, oxidizer, O/F, p_c)
> c* CEA = combustion.cstar
> Mm CEA = combustion.Mm
> combustion products = combustion.products
> combustion products mass percentage = combustion.products_wt%

> for every combustion product:
  » from NIST download tabulated thermal properties
  » return thermal properties
> for every tabulated Θ:
  » γ = sum(γ · product %) / 100
  » return γ

> $\gamma(\Theta)$ = polynomial fit(7th order, γ, Θ)
> d$\gamma(\Theta)$/dΘ = derivative_function($\gamma(\Theta)$)

4.3 Compute new throat area

This section introduces the core of the algorithm, organized in layers. The following paragraphs represent those layers, from the most external to the inner layer.

4.3.1 Outer level function: Z_obj

The highest level consists in a minimization problem, where the error function $Z\_obj(^*args)$ is defined such that if $Z\_obj(^*args) = 0$, then $^*args$ are the solution to the problem. The error function is defined as the normalized error with respect to the computed and experimental chamber pressure and thrust at exit:

$$\boldsymbol{Z\_obj(^*args)} = \begin{bmatrix} \frac{p_{c,\,exp} - p_c(^*args)}{p_{c,\,exp}} \\ \frac{T_{exp} - T(^*args)}{T_{exp}} \end{bmatrix} \qquad [14]$$

Here, if $\boldsymbol{Z\_obj(^*args)} = 0$, then $p_c(^*args) = p_{c,\,exp}$ and $T(^*args) = T_{exp}$, meaning that the input $^*args$ are the correct arguments to match computed values with experimental values. Since $\boldsymbol{Z\_obj(^*args)}$ is defined by two equations, $^*args$ must consist of exactly 2 variables (or unknowns) to have a closed problem. Those two variables are chosen as the throat temperature (Θ_{th}) and the throat area (A_{th}), which is a convenient choice as explained later. Thus, the generic input arguments are redefined as:

$$^*args = \begin{bmatrix} A_{th} & \Theta_{th} & ^*constants \end{bmatrix} \qquad [15]$$

where $^*constants$ represent the extra parameters introduced earlier and explained in the subsequent paragraph. The goal is to find the throat area and throat temperature such that the error function is minimized to nearly zero.

Syntax logic:

> define Z_obj(A_th, Θ_th, *constants)
  » p_c, T = nozzle_solver(A_th, Θ_th, *constants)
  » Z(1) = (p_c real - p_c) / p_c real
  » Z(2) = (T real - T) / T real
  return Z

> find A_th and Θ_th | Z_obj(A_th, Θ_th, *constants)$\sim$0

Next paragraph explores how the mentioned $nozzle\_solver$ function is built.

4.3.2 Mid level function: nozzle_solver

The mid-level function, $nozzle\_solver$, is responsible for relating the throat area (A_{th}) and throat temperature (Θ_{th}) to the chamber pressure (p_c) and thrust (T). The following principles are used:

- Conservation of mass.
- Perfect gas law.
- Throat choking condition.
- Shapiro's equations.

With throat area and temperature provided as input (initial guess values), the sonic flow speed can be computed as:

$$a_{th} = \sqrt{\gamma(\Theta_{th}) \cdot R \cdot \Theta_{th}} \qquad [16]$$

where γ is passed as a function of Θ in the $^*constants$, and R is the specific gas constant, calculated as $R = R_u/Mm$, where Mm (molar mass) is assumed constant (frozen mixture) and also passed in the $^*constants$.

where γ is passed as function of Θ in the $^*constants$ and R is the perfect gas constant $R = R_u/Mm$, with Mm constant under the hypothesis of frozen mixture and passed in the $^*constants$ as well. Using the throat choking condition, where the Mach number (Ma) is 1, the actual gas flow speed at the throat is:

$$Ma_{th} = 1 \qquad \rightarrow \qquad v_{th} = a_{th} \qquad [17]$$

From the conservation of mass, the gas density at the throat is:

$$\rho_{th} = \frac{\dot{m}_{tot,\,exp}}{A_{th}\; v_{th}} \qquad [18]$$

where $\dot{m}_{tot,\,exp}$ is the experimental total mass flow rate, passed in $^*constants$. Finally, the pressure at the throat can be obtained using the ideal gas law:

$$p_{th} = \rho_{th}\; R\; \Theta_{th} \qquad [19]$$

Now that the throat gas properties are characterized, the gas properties vector $\boldsymbol{y}$ is defined as:

$$\boldsymbol{y} = \begin{bmatrix} Ma^2 & v & a & \Theta & \rho & p & F & s \end{bmatrix} \qquad [20]$$

in line with Shapiro's formulation [32]. Indeed, the differential form of the gas properties $\boldsymbol{y}$ along the nozzle can be correlated to their state $\boldsymbol{y}$ by the use of Shapiro's equations:

$$\frac{\partial \boldsymbol{y}}{\partial z} = ode\_Shapiro(\boldsymbol{y}, ^{*}constants) \qquad [21]$$

where z is the nozzle axial coordinate (or normalized coordinate), and the function $Ode\_Shapiro$ is described in the next paragraph. By integrating from the throat ($z = 0$) to the combustion chamber ($z = -1$) starting from the vector at the throat $\boldsymbol{y_{th}} = \left[Ma^2_{th,\,\epsilon} \quad v_{th} \quad a_{th} \quad \Theta_{th} \quad \rho_{th} \quad p_{th} \quad - \quad -\right]$ the combustion chamber status vector $\boldsymbol{y_c}$ is found. Similarly, by integrating from the throat to the nozzle exit ($z = 1$), the exit status vector $\boldsymbol{y_e}$ is obtained. The Mach number $Ma_{th,\,\epsilon}$ is equal to $Ma_{th} - \epsilon$ for the throat to chamber integration, and $Ma_{th} + \epsilon$ for the throat to exit integration ensuring subsonic and supersonic condition respectively. Here, ϵ is a small value that helps overcome the numerical singularity at $Ma = 1$ in Shapiro's equations. The chamber status vector $\boldsymbol{y_c}$ contains one of the desired outputs, p_c. Thrust (T) is computed using:

$$T = \dot{m}_{tot,\,exp} \cdot v_e \cdot \lambda + (p_e - p_{amb}) \cdot A_e \qquad [22]$$

where v_e and p_e are contained in $\boldsymbol{y_e}$, A_e is the nozzle exit area, p_{amb} is the ambient pressure at the exit, and λ is the corrective factor for 3D losses, which is 1 if they are not considered. For a conical nozzle with a semi-angle ($\alpha = 10°$ in this setup), λ is calculated as:

$$\lambda = 0.5 \cdot (1 + \cos(\alpha)) \qquad [23]$$

Starting from the throat has several advantages: it allows the use of mass conservation and the choking condition more directly, and it provides better initialization for the integration of Shapiro's equations due to the known Mach number at the throat.

Syntax logic:

> define nozzle_solver(A_th, Θ_th, *constants)
» Θ = Θ_th
» a = sqrt(γ(*Theta*) · R · Θ)
» Mach = 1
» v = Mach · a
» ρ = mass flow rate real / (A_th · v)
» p = ρ · R · Θ
» y_th = [0.99..9, v, a, Θ, ρ, p, 0, 0]
» z = [0, -1]
» y_c = integrate(function=ode_Shapiro(y), in z, from y_th)
» y_th = [1.00..1, v, a, Θ, ρ, p, 0, 0]
» z = [0, 1]
» y_e = integrate(function=ode_Shapiro(y), in z, from y_th)
» p_c = y_c(6)
» T = mass flow rate real · y_e(2) · λ + (y_e(6)-p_amb) · A_e
return p_c, T

4.3.3 Inner layer function: ode_Shapiro

The function $ode\_Shapiro$ correlates the gas status vector, $\boldsymbol{y}$, with its partial derivative with respect to the nozzle's axial coordinate, as described in Eq. [21]. This is achieved by applying Shapiro's equations, with certain additional considerations for nozzle flow dynamics. Shapiro's equations, describe the gas properties along the nozzle. The independent variables ($\boldsymbol{x}$) represent the following:

- Nozzle section (A).
- Heat, work, enthalpy.
- Friction effects.
- Mass flow rate ($\dot{m}$).
- Molecular weight (Mm).
- Specific heat ratio (γ).

Shapiro correlates the normalized partial derivatives of $\boldsymbol{x}$ and $\boldsymbol{y}$ as follows:

$$\frac{\partial \boldsymbol{x}}{\boldsymbol{x}} = \begin{bmatrix} \frac{\partial A}{A} \\ \frac{\partial q - \partial W x + \partial H}{c_p \cdot \Theta} \\ \frac{4 \cdot f \cdot \partial x}{D} + \frac{\partial X}{0.5 \cdot k_p \cdot A \cdot M^2} - 2y \cdot \frac{\partial \dot{m}}{\dot{m}} \\ \frac{\partial \dot{m}}{\dot{m}} \\ \frac{\partial Mm}{Mm} \\ \frac{\partial \gamma}{\gamma} \end{bmatrix} \qquad [24]$$

$$\frac{\partial \boldsymbol{y}}{\boldsymbol{y}} = \begin{bmatrix} \frac{\partial Ma^2}{Ma^2} & \frac{\partial v}{v} & \frac{\partial a}{a} & \frac{\partial \Theta}{\Theta} & \frac{\partial \rho}{\rho} & \frac{\partial p}{p} & \frac{\partial F}{F} & \frac{\partial s}{c_p} \end{bmatrix}' \qquad [25]$$

$$\frac{\partial \boldsymbol{y}}{\boldsymbol{y}} = \boldsymbol{M}(Ma^2,\, \gamma) \cdot \frac{\partial \boldsymbol{x}}{\boldsymbol{x}} \qquad [26]$$

where $\boldsymbol{M}$ is a matrix function of the Mach number squared (Ma^2) and the specific heat ratio (γ) [32]. Knowing $\boldsymbol{y}$ and $\partial \boldsymbol{x}/\boldsymbol{x}$ allows to compute $\partial \boldsymbol{y}$. Let's now examine how these relations are used in the presented algorithm, from the last term of $\partial \boldsymbol{x}/\boldsymbol{x}$ to the first:

- Specific heat ratio (γ) and its derivative are known as functions of temperature (as discussed in Section 4.2). Since the status vector $\boldsymbol{y}$ contains temperature (Θ), this can be evaluated at any given state.
- Molar mass (Mm) is constant in this model (frozen mixture), so its derivative is zero.
- Mass flow rate is also constant, meaning its derivative is zero as well.

- Friction is assumed to be negligible, so the corresponding term is set to zero, as friction effects are minimal in typical nozzle applications of this kind.
- Heat exchange (∂q) is considered due to the heat losses along the nozzle, and there is no work or enthalpy variation ($Wx = 0$, $H = 0$).
- sectional variation ($\partial A/A$) is known based on the nozzle geometry.

Thus, Eq. [24] simplifies to:

$$\frac{\partial \boldsymbol{x}}{\boldsymbol{x}} = \begin{bmatrix} \frac{\partial A}{A} & \frac{\partial q}{c_p \cdot \Theta} & 0 & 0 & 0 & \frac{\partial \gamma}{\gamma} \end{bmatrix}' \quad [27]$$

At any axial position z, the values of $\boldsymbol{x}$ and $\partial \boldsymbol{x}$ are always known. If the initial condition $\boldsymbol{y}_{z_0}$ is partially known (with at least Ma^2 and Θ, necessary for $\boldsymbol{M}$), $\partial \boldsymbol{y}$ can be computed and integrated along z to obtain the full status vector $\boldsymbol{y}(z)$.

An important note involves handling the variation of γ. The derivatives are computed with respect to z, whereas γ is expressed as a function of temperature (Θ). To address this,the chain rule is applied:

$$\frac{\partial \gamma}{\partial z} = \frac{\partial \gamma}{\partial \Theta} \cdot \frac{\partial \Theta}{\partial z} \quad [28]$$

In informal terms:

$$\partial \gamma(z) = \partial \gamma(\Theta) \cdot \partial \Theta(z) \quad [29]$$

Initially, Shapiro's matrix $\boldsymbol{M}$ is solved assuming $\partial \gamma = 0$. This allows to compute the correct $\partial \Theta$ with respect to z, which is not function of $\partial \gamma$. It is then used to compute $\partial \gamma(z)$ via Eq. [29]. Afterward, Shapiro's equations are solved a second time, accounting for the correct variation of γ, yielding the final solution.

Syntax logic:

> define ode_Shapiro(z, y in z, *constants)
» A(z) = constants.A
» dA(z) = constants.dA
» $\gamma(\Theta)$ = constants.γ
» $d\gamma(\Theta)$ = constants.dγ
» dq(z) = constants.dq
» Mm = constans.Mm
» evaluate values for current z and current Theta

» R = R_u / Mm
» cp = R · γ / (γ-1)
» Shapiro (first round, dγ=0):
» dx over x = [dA/A, dq / (cp · Θ), 0, 0, 0, 0]
» dy over y = M(y(1)^2, γ) · dx over x
» dy(1 : end-1) = dy over y (1 : end-1) · y(1 : end-1)
» dy(end) = dy over y (end) · cp
» return dy
» dΘ = dy over y (4)
» dγ in z = dγ in Θ · dΘ
» Shapiro (second round, d$\gamma \neq 0$):
» ...
return dy
return dy

4.4 Post processing

At this stage, the nozzle throat area and combustion chamber temperature that satisfy the target chamber pressure and measured thrust have been determined. Running the $nozzle\_solver$ function with these values provides the gas flow state along the entire nozzle axis, of which an example is shown in Fig. 2). The characteristic velocity, c^*, as defined in Eq. [13], can be evaluated using both the geometrical throat area and the newly computed throat area. These two characteristic velocities are referred to as c^*_{old} and c^*_{new}. With these values, the combustion efficiency can be computed using Eq. [12]. The combustion efficiency is calculated for both the old and new characteristic velocities, allowing for a comparison between the standard and the new method.

5. Results

The experimental campaign was conducted using the VFP engine with the fuels listed in Tab. 1, combined with oxygen as the oxidizer. Various mass flow rates were employed to explore multiple oxidizer-to-fuel (O/F) ratios and total mass flux conditions. The theoretical burning time was adjusted during different tests to avoid overstressing the engine and to preserve some residual fuel mass for post-processing. This adjustment also took into account the mechanical properties of the fuels, where faster-burning fuels were fired for shorter durations. Additionally, a general rule of thumb was applied: burning time was reduced when the oxidizer mass flow rate was higher, to ensure balanced grain consumption. The main outcomes of the experimental campaign are summarized in Tab. 3.

5.1 Ballistic Analysis

The regression rate and total mass flux are calculated according to Eqs. [5] and [9], and they are related by the power law:

$$r_f = a_r \, G_{tot}^{n_r} \quad [30]$$

Since r_f and G_{tot} are known for each test, the coefficients a_r and n_r are determined through fitting, resulting in a power law specific to each fuel formulation. The data presented in this paper are supplemented with test results from previous studies [1]. The results are summarized in Fig. 3 and Tab. 2. The ballistic analysis highlights the im-

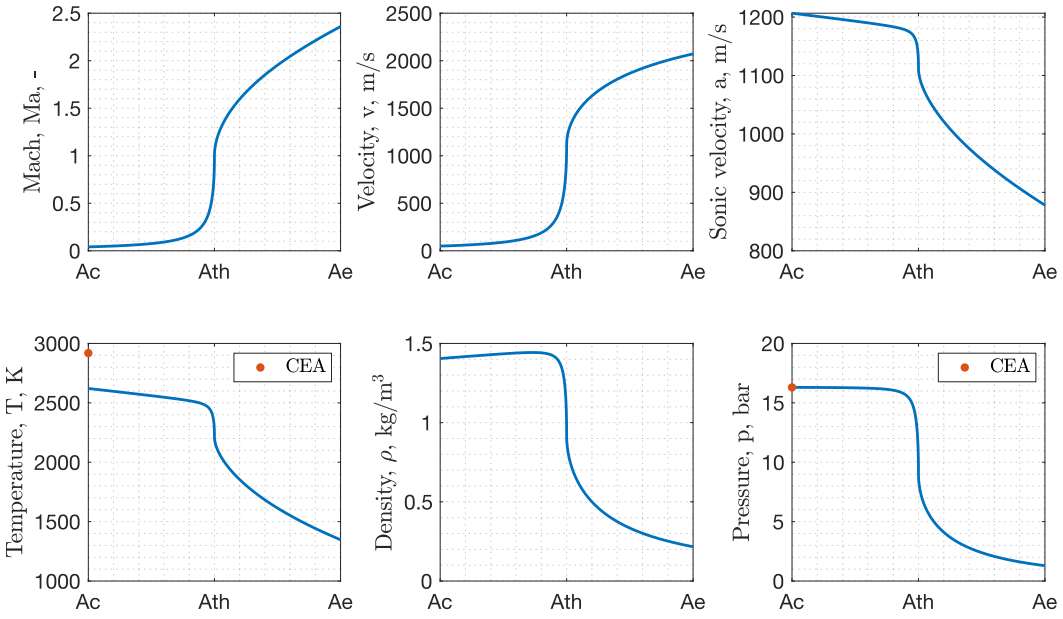

Fig. 2. Example of gas properties evolution along the nozzle, accounting for heat and conical losses.

pact of the entrainment effect on the regression rate: ABS is the slowest-burning formulation, while in paraffin-based fuels, the regression rate increases as the SEBS-MA percentage decreases, corresponding to lower viscosity. However, it should be noted that pure paraffin (W1) exhibits scattered data and a relatively low coefficient of determination.

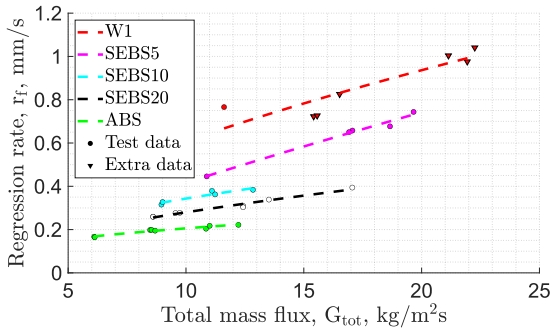

Fig. 3. Regression rate as function of the total mass flux.

5.2 Combustion Efficiencies

The developed algorithm consistently proved effective, achieving a 100% convergence rate. The last four columns of Tab. 3 provide the following data: (i) $\zeta_{A_{th}}$, the ratio between the reduced throat area and the geometrical one; (ii) $\zeta_{\Theta_{fl}}$, the ratio between the estimated flame temperature and the adiabatic flame temperature; (iii) $\eta_{c^*_{old}}$, the standard combustion efficiency; and (iv) $\eta_{c^*_{new}}$, the combustion efficiency computed using the new throat area. In six tests, $\zeta_{\Theta_{fl}}$ was greater than 1, which is physically impossible; therefore, these solutions were discarded despite successful convergence. This discrepancy is likely due to experimental measurement errors. All remaining results fully align with expectations, showing a reduced throat area, a lower chamber temperature than the adiabatic flame temperature, and a new combustion efficiency lower than that calculated by the standard method. A visual representation of combustion efficiency comparison is shown in Fig. 4. The difference between the two com-

Table 2. Regression rate coefficients and coeffient of determination.

Fuel	$\mathbf{a_r}$ $\left[\frac{\mathbf{mm/s}}{(\mathbf{kg/m^2s})^{\mathbf{nr}}}\right]$	$\mathbf{n_r}$ [−]	$\mathbf{R^2}$ [−]
ABS	0.0633	0.5179	0.9664
SEBS5	0.0609	0.8347	0.9844
SEBS10	0.0995	0.5371	0.8930
SEBS20	0.0738	0.5803	0.9683
W1	0.1709	0.5648	0.7868

bustion efficiencies ranges from a minimum of 4.38% in the W1 firing test to a maximum of 13.74% in one of the SEBS5 tests. Generally, the new combustion efficiencies are significantly lower than those typically expected from a swirled injection engine [4–11]. However, the developed algorithm is a preliminary version based on a fully chemically frozen expansion, which tends to underestimate the parameter of interest. Accounting for heat losses and conical nozzle losses increases the computed $\eta_{c^*_{new}}$ by approximately 0-2% compared to when these losses are ignored, although the shape of the function $\partial q(z)/\partial z$ has minimal impact on the result.

It is beneficial to track both the old and new combustion efficiencies, as they together represent the lower and upper limits of the actual value. Fig. 5 illustrates this with error bars centered at average values, plotted as a function of total mass flow rate, with different colors representing various fuel formulations.

Lastly, pressure was measured at both the injection arm and the bottom of the combustion chamber at the center of the vortex, to verify and account for the centrifugal effect, which could potentially bias pressure measurements and impact combustion efficiency [18]. However, no differences were observed between the measurements from the two pressure sensors, as shown in Fig. 1a.

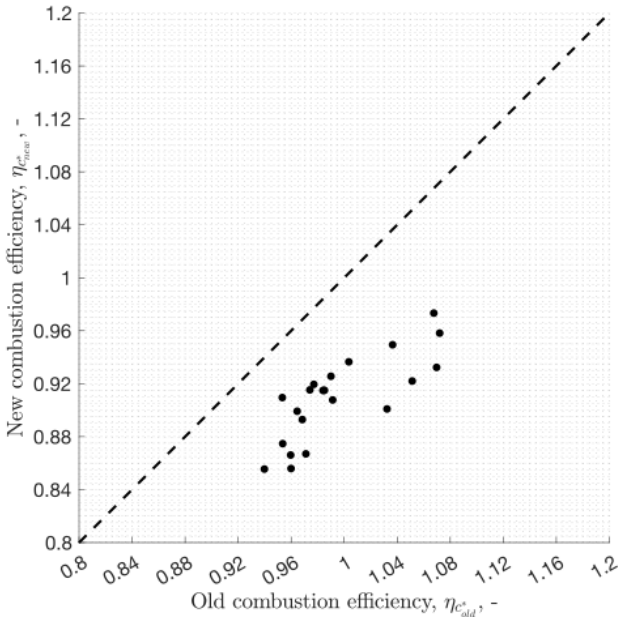

Fig. 4. Comparison between the old and new combustion efficiency.

6. Conclusions

This research developed an innovative methodology for calculating combustion chamber efficiency in the presence of swirling gas flows. When gas is accelerated through the nozzle, the effective nozzle area contracts, causing standard evaluation methods to overestimate η_{c^*}. The developed algorithm introduces an additional measurement, thrust, to calculate throat shrinkage. The gas flow is treated as one-dimensional and chemically frozen, but the combustion mixture is modeled as a calorically imperfect gas using NASA-CEA code and NIST data. The nozzle's thermo-fluid dynamic is solved using Shapiro's differential equations to accurately account for heat losses. This preliminary version achieved a 100% convergence rate, successfully matching all experimental data.

The algorithm was applied during an experimental test campaign on the VFP engine at the Space Propulsion Laboratory of Politecnico di Milano, an engine characterized by strongly swirled injection flow. Multiple firing tests were conducted with different fuel formulations, measuring chamber pressure at the injection point and the centerhead of the combustion chamber, thrust, mass flow rate, and cooling water temperature. These data were used for ballistic analysis and to calculate gas heat losses.

The dual pressure measurement was performed to verify the effect of the swirling flow on the pressure sensor due to centrifugal forces. However, no differences were observed in the tests. The combustion efficiencies calculated with the new method were consistently lower than those determined by standard methods, as expected from the literature, with differences ranging from 4.38% to 13.74%. Ignoring heat losses or conical-nozzle corrections in the proposed method lowers the calculated combustion efficiency by 0–2% in the tested setup, while the distribution of heat losses along the nozzle axis has a negligible impact The results establish a lower limit for combustion efficiency in engines with swirl injection.

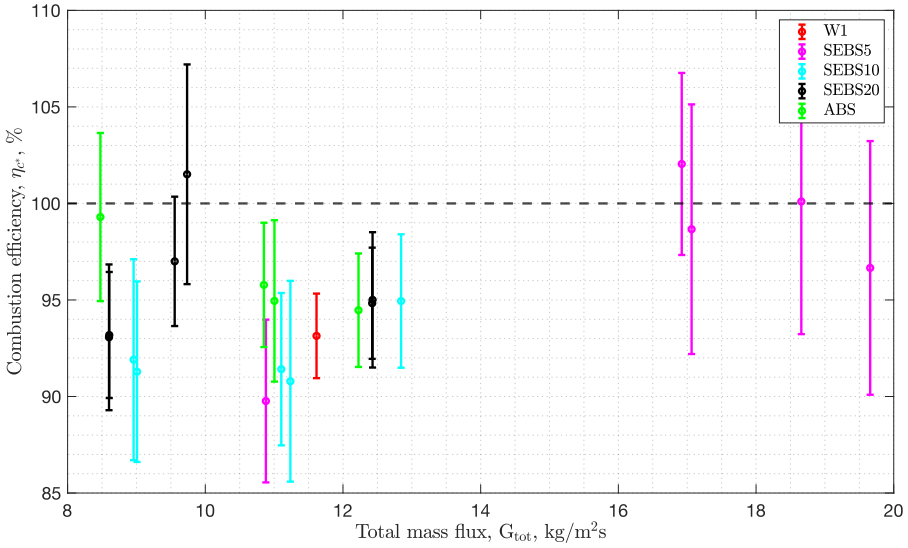

Fig. 5. Average combustion efficiency and its limits function of the total mass flux, divided by fuel type.

Table 3. Experimental results of the test campaign.

Fuel	ε -	$\bar{p}$ MPa	Δt_b s	$\bar{T}$ N	$\dot{Q}$ kW	$\dot{\bar{m}}_{tot}$ g/s	$\bar{G}_{tot}$ kg/m^{2}s	r_f mm/s	$\zeta_{A_{th}}$ -	$\zeta_{\Theta_{fl}}$ -	$\eta_{c^*_{old}}$ %	$\eta_{c^*_{new}}$ %
ABS	2.00	0.70	14.18	14.59	NA	8.19	8.48	0.20	0.92	0.91	103.65	94.94
ABS	2.00	0.72	13.33	15.75	NA	8.20	8.54	0.20		>1		
ABS	2.00	0.72	10.93	16.17	6.120	8.19	8.69	0.20		>1		
ABS	2.00	0.51	15.50	10.22	4.800	5.85	6.11	0.17		>1		
ABS	2.00	0.51	14.26	10.23	4.120	5.82	6.13	0.16		>1		
ABS	2.00	0.85	11.30	18.78	6.350	10.79	10.85	0.20	0.93	0.92	99.00	92.56
ABS	2.00	0.87	10.84	18.96	5.940	10.95	11.00	0.22	0.92	0.88	99.13	90.77
ABS	2.00	0.93	9.69	21.15	6.490	12.12	12.23	0.22	0.94	0.89	97.41	91.53
W1	2.00	0.83	14.97	18.56	4.020	13.63	11.62	0.77	0.95	0.79	95.33	90.95
W1SEBS5	2.00	1.63	7.67	37.35	9.160	17.63	17.06	0.66	0.88	0.90	105.13	92.20
W1SEBS5	2.00	1.65	7.78	39.22	9.370	18.15	17.66	0.65	0.87	0.89	105.14	91.79
W1SEBS5	2.00	1.86	7.99	43.10	10.360	19.46	18.66	0.68	0.87	0.91	106.97	93.23
W1SEBS5	2.00	1.90	7.71	43.93	11.780	20.67	19.66	0.74	0.87	0.86	103.23	90.09
W1SEBS5	2.00	0.96	12.83	20.86	9.280	11.80	10.88	0.45	0.91	0.81	93.98	85.55
W1SEBS10	2.00	0.83	14.63	17.34	4.790	9.59	8.96	0.32	0.89	0.80	97.11	86.70
W1SEBS10	2.00	0.82	14.72	17.31	4.320	9.63	9.01	0.33	0.90	0.79	95.96	86.61
W1SEBS10	2.00	1.00	11.45	22.46	5.800	11.78	11.10	0.38	0.92	0.81	95.36	87.47
W1SEBS10	2.00	0.99	9.92	21.53	5.600	11.58	11.24	0.36	0.89	0.78	95.99	85.59
W1SEBS10	2.00	1.17	10.29	27.32	6.640	13.42	12.84	0.38	0.93	0.88	98.40	91.49
W1SEBS20	2.00	1.38	13.21	32.33	13.670	14.49	13.52	0.34		>1		
W1SEBS20	2.00	1.56	4.37	37.76	11.560	16.93	17.06	0.39		>1		
W1SEBS20	2.00	0.91	16.84	20.36	9.920	10.37	9.56	0.28	0.93	0.96	100.35	93.65
W1SEBS20	2.00	0.92	14.77	19.70	9.690	9.80	9.74	0.28	0.89	1.00	107.20	95.82
W1SEBS20	2.00	0.78	15.12	16.98	5.240	9.20	8.60	0.26	0.93	0.86	96.45	89.92
W1SEBS20	2.00	0.77	14.93	16.47	5.530	9.04	8.60	0.26	0.92	0.85	96.84	89.29
W1SEBS20	2.00	1.09	10.12	25.16	6.830	12.88	12.43	0.31	0.93	0.88	98.51	91.50
W1SEBS20	2.00	1.08	9.65	25.07	6.760	12.85	12.42	0.30	0.94	0.89	97.71	91.95

[1] V. Santolini, R. Bisin, F. Giambelli, and C. Paravan, "An overview of splab activities on vortex combustion in a non-conventional hybrid rocket engine," in *The Thirteenth International Symposium on Special Topics in Chemical Propulsion and Energetic Materials (13-ISICP)*, Gjøvik, Norway, 2023.

[2] N. Bellomo, F. Barato, F. Faenza, M. Lazzarin, A. Bettella, and D. Pavarin, "Numerical and experimental investigation of unidirectional vortex injection in hybrid rocket engines," *Journal of Propulsion and Power*, vol. 29, no. 5, pp. 1097–1113, 2013. DOI: 10.2514/1.B34506.

[3] I. Nakagawa, D. Kishizato, Y. Koinuma, and S. Tanaka, "Demonstration of an altering-intensity swirling-oxidizer-flow-type hybrid rocket function," *Journal of Propulsion and Power*, vol. 37, no. 2, pp. 326–331, 2021. DOI: 10.2514/1.B37915.

[4] W. Knuth, M. Chiaverini, D. Gramer, and J. Sauer, "Experimental investigation of a vortex-driven high-regression rate hybrid rocket engine," in *34th AIAA/ASME/SAE/ASEE Joint Propulsion Conference & Exhibit*, Cleveland, OH, USA, 1998. DOI: 10.2514/6.1998-3348.

[5] W. Knuth, D. Gramer, M. Chiaverini, and J. Sauer, "Development and testing of a vortex-driven, high-regression rate hybrid rocket engine," in *34th AIAA/ASME/SAE/ASEE Joint Propulsion Conference & Exhibit*, Cleveland, OH, USA, 1998. DOI: 10.2514/6.1998-3507.

[6] W. H. Knuth, M. J. Chiaverini, J. A. Sauer, and D. J. Gramer, "Solid-fuel regression rate behavior of vortex hybrid rocket engines," *Journal of Propulsion and Power*, vol. 18, no. 3, pp. 600–609, 2002. DOI: 10.2514/2.5974.

[7] Y. Saburo, S. Noriko, and H. Kousuke, "Controlling parameters for fuel regression rate of swirling-oxidizer-flow-type hybrid rocket engine," in *48th AIAA/ASME/SAE/ASEE Joint Propulsion Conference & Exhibit*, Atlanta, Georgia, 2012. DOI: 10.2514/6.2012-4106.

[8] B. Vignesh and R. Kumar, "Effect of multi-location swirl injection on the performance of hybrid rocket motor," *Acta Astronautica*, vol. 176, pp. 111–123, 2020. DOI: 10.1016/j.actaastro.2020.06.029.

[9] G. S. Haag, "Alternative geometry hybrid rockets for spacecraft orbit transfer," Ph.D. dissertation, University of Surrey (United Kingdom), 2001.

[10] D. M. Gibbon and G. S. Haag, "Investigation of an alternative geometry hybrid rocket for small spacecraft orbit transfer," *SURREY SATELLITE TECHNOLOGY LTD GUILDFORD (UNITED KINGDOM)*, 2001.

[11] A. Hashish, C. Paravan, and A. Verga, "Liquefying fuel combustion in a lab-scale vortex flow pancake hybrid rocket engine," in *AIAA Propulsion and Energy 2021 Forum*, ONLINE, 2021. DOI: 10.2514/6.2021-3519.

[12] A. Mager, "Approximate solution of isentropic swirling flow through a nozzle," *ARS Journal*, vol. 31, no. 8, pp. 1140–1148, 1961. DOI: 10.2514/8.5732.

[13] A. D. Cutler and R. W. Barnwell, "Vortex flow in a convergent-divergent nozzle," *AIAA Journal*, vol. 37, no. 10, pp. 1329–1331, 1999. DOI: 10.2514/2.606.

[14] A. Gany, M. Mor, and C. Goldman, "Analysis and characteristics of choked swirling nozzle flows," *AIAA Journal*, vol. 43, no. 10, pp. 2177–2181, 2005. DOI: 10.2514/1.16887.

[15] A. Abdelhafez and A. K. Gupta, "Swirling airflow through a nozzle: Choking criteria," *Journal of Propulsion and Power*, vol. 26, no. 4, pp. 754–764, 2010. DOI: 10.2514/1.47956.

[16] C. Goldman and A. Gany, "Thrust modulation of ram-rockets by a vortex valve," in *32nd Joint Propulsion Conference & Exhibit*, Lake Buena Vista, FL, USA, 1996. DOI: 10.2514/6.1996-2624.

[17] S. Yuasa, N. Shiraishi, M. Sakamoto, C. Sezaki, K. Hirata, and T. Sakurai, "Evaluation method of c* efficiency of swirling-oxidizer-flow-type hybrid rocket engines," *Japan Society of Aeronautical Space Sciences*, vol. 59, no. 687, pp. 97–101, 2011. DOI: 10.2322/jjsass.59.97.

[18] K. Ozawa, K. Kitagawa, S. Aso, and T. Shimada, "Hybrid rocket firing experiments at various axial–tangential oxidizer-flow-rate ratios," *Journal of Propulsion and Power*, vol. 35, no. 1, pp. 94–108, 2019. DOI: 10.2514/1.B36889.

[19] R. Bisin, C. Paravan, S. Alberti, and L. Galfetti, "A new strategy for the reinforcement of paraffin-based fuels based on cellular structures: The armored grain – mechanical characterization," *Acta Astronautica*, vol. 176, pp. 494–509, 2020. DOI: 10.1016/j.actaastro.2020.07.003.

[20] R. Bisin, A. Verga, D. Bruschi, and C. Paravan, "Strategies for paraffin-based fuels reinforcement: 3d printing and blending with polymers," in *AIAA Propulsion and Energy 2021 Forum*, Online, 2021. DOI: 10.2514/6.2021-3502.

[21] S. A. Whitmore, Z. W. Peterson, and S. D. Eilers, "Comparing hydroxyl terminated polybutadiene and acrylonitrile butadiene styrene as hybrid rocket fuels," *Journal of Propulsion and Power*, vol. 29, no. 3, pp. 582–592, 2013. DOI: 10.2514/1.B34382.

[22] S. Whitmore, Z. Peterson, and S. Eilers, "Analytical and experimental comparisons of htpb and abs as hybrid rocket fuels," in *47th AIAA/ASME/SAE/ASEE Joint Propulsion Conference & Exhibit*, San Diego, CA, USA, 2012. DOI: 10.2514/6.2011-5909.

[23] J. R. Wilson and S. A. Whitmore, "Pyrolysis of acrylonitrile-butadiene-styrene (abs) under high heat flux conditions," in *50th AIAA/ASME/SAE/ASEE Joint Propulsion Conference*, Cleveland, OH, USA, 2014. DOI: 10.2514/6.2014-3752.

[24] M. Freund, R. Csikós, S. Keszthely, and G. Y. Mózes, *Paraffin products: properties, technologies, applications*. Amsterdam-Oxford-New York: Elsevier, 1982.

[25] U. Wolfmeier *et al.*, "Waxes," *Ullmann's Encyclopedia of Industrial Chemistry*, 2015. DOI: 10.1002/14356007.a28_103.pub2.

[26] *Sasol: Sasolwax 0907*, https://www.sasol.com/sasolwax-0907, Last accessed 10 april 2024.

[27] M. A. Karabeyoglu, D. Altman, and B. J. Cantwell, "Combustion of liquefying hybrid propellants: Part 1, general theory," *Journal of Propulsion and Power*, vol. 18, no. 3, pp. 610–620, 2002. DOI: 10.2514/2.5975.

[28] *Sigma-aldrich: Sebs-ma*, https://www.sigmaaldrich.com/IT/it/product/aldrich/432431?context=product, Last accessed 10 april 2024.

[29] C. Paravan, L. Galfetti, and F. Maggi, "A critical analysis of paraffin-based fuel formulations for hybrid rocket propulsion," in *53rd AIAA/SAE/ASEE Joint Propulsion Conference*, Atlanta, GA, USA, 2017. DOI: 10.2514/6.2017-4830.

[30] *Sigma-Aldrich: Grafite*, https://www.sigmaaldrich.com/IT/it/product/aldrich/282863?context=product, Last accessed 10 april 2024.

[31] V. Santolini and C. Paravan, "Combustion in a non-conventional hybrid rocket engine: Lab-scale testing of a vortex flow pancake," in *Space Propulsion*, Glasgow, Scotland, UK, 2024.

[32] A. H. Shapiro, *The Dynamics and Thermodynamics of Compressible Fluid Flow*. John Wiley & Sons, 1953, vol. 1, ch. 8, p. 228.